Electromagnetic Science
vol. 2, no. 4, 0080282, December 2024
https://doi.org/10.23919/emsci.2024.0028

Research Article

Theory of Periodic Sequence: A Generalized Formalism of Maxwell's Equations in Discrete Transform Domain

Ben You and Ke Wu

Poly-Grames Research Center and Department of Electrical Engineering, *Polytechnique Montreal*, *Montreal*, *QC H3T 1J4*, *Canada*

Corresponding author: Ke Wu, Email: ke.wu@polymtl.ca.
Received May 30, 2024; Accepted October 24, 2024; Published Online November 13, 2024.

Abstract — Time-periodic form or expression is commonly observed in both natural and man-made phenomena across a wide range of scientific and engineering disciplines. In this article, we propose the theory of periodic sequence (TPS), marking the first effort to mathematically formalize Maxwell's equations in the discrete transform domain (corresponding to time domain) and to legitimize the application of the discrete Fourier transform to the temporal aspect of Maxwell's equation. TPS is intended to serve as a comprehensive theory to depict the physical behavior of electromagnetic (EM) periodic sequential fields and waves. Within the TPS framework, periodic-sequential Maxwell's curl equations are decomposed and decoupled to independent and paralleled instances via designated mappings. The fundamental solutions of EM periodic sequential excitation are elucidated and corroborated by radio-frequency (RF)/microwave measurements. This involves potential applications in the analysis of broadband RF transmission and the design of high-speed RF devices.
Keywords — Theory of periodic sequence , Time-periodic electromagnetics, Broadband transmission.
Citation — Ben You and Ke Wu, "Theory of periodic sequence: A generalized formalism of Maxwell's equations in discrete transform domain," *Electromagnetic Science*, vol. 2, no. 4, article no. 0080282, 2024. doi: 10.23919/emsci.2024.0028.

I. Introduction

Time-periodic phenomena can be commonly observed in the natural world and the engineering field. In fact, such a time-scale periodicity or periodic sequence that inherently characterizes parametric motions, dynamics, and evolutions, presents fundamental features and phenomena in the disciplines of physics and others including electrodynamics [1], [2], acoustics [3]–[5], thermodynamics [6]–[8], and quantum mechanics [9]–[11]. With the fast development of today's computers and computing techniques, any natural and engineered dynamics such as the propagation of waves can be easily described and explained by temporal-spatial sequences in terms of Fourier decompositions or compositions. In this connection, it inspires and guides us to utilize specific periodic sequences of choice for developing theories of physics, especially for electromagnetic (EM) wave equations under time-periodic boundary conditions (TPBCs).

TPBC is associated with continuous time-periodic EM waves featuring diverse waveforms, covering all periodic waves characterized by arbitrary shapes. These waves possess the capacity to carry more valuable signal information than sinusoids, showcasing promising potential in advancing the development of a high-speed computational EM platform. For such EM problems, time-domain methods, such as finite-difference time-domain (FDTD) method [12], wavelet transform [13], and Laguerre polynomials [14], are barely suitable due to the periodic nature.

On the other hand, frequency-domain methods, such as finite-difference frequency-domain (FDFD) method [15], method of moments (MoM) [16] and finite element method (FEM) [17], are based on sinusoidal signals, which can be viewed as the result of applying continuous-time Fourier transform (CTFT) to Maxwell's curl equations [18]–[22]. Furthermore, any arbitrary continuous time-periodic EM wave can be decomposed into an infinite set of spectral components in the frequency domain. Subsequently, the frequency-domain wave equation is employed to derive the response corresponding to each component, using the

inverse CTFT to obtain the time-domain waveform of a given periodic excitation. While the CTFT conceptually possesses an infinite period in mathematics, modern computational science and communications in the computer era heavily rely on discretization, which involves finite periods.

For practical applications, researchers and engineers frequently employ the fast Fourier transform (FFT) to extract the excitation spectrum of continuous time-periodic EM waves. They then apply frequency-domain Maxwell's equations to address the propagation problem of EM periodic sequences and subsequently derive its temporal response via inverse FFT (IFFT). We must mention that both FFT and IFFT operate on periodic sequences rather than continuous time-periodic signals. From a rigorous mathematical standpoint, for an accurate representation of the propagation problem of EM periodic sequences, it is necessary to develop a new form of Maxwell's equations that fully incorporates discretization for the time-related components.

Table 1 shows a comparison of the aforementioned algorithms based on EM signal types and domain categories. It is evident that a rigorous EM theory is absent in the lower-right corner (highlighted in green). To fill up this gap, we have endeavored to develop a generalized discrete Fourier transform (DFT) version of Maxwell's equations to describe the propagation of periodic-sequential EM waves, leading to the formulation of our proposed theory.

Traditionally, the concept of DFT is primarily associated with field transformations rather than being applied to the full set of partial differential equations (PDEs) in science and engineering. In our work, we extend this concept to encompass the entire set of Maxwell's equations, thereby providing a more comprehensive understanding of the underlying principles that link time-domain and frequency-domain formalisms and solutions.

In this article, we introduce a distinctive computational methodology called the theory of periodic sequence (TPS). This methodology is designed to effectively tackle the state-steady process of time-periodic EM fields and waves. We will reveal and elucidate an intriguing and inherent property of TPS: The computational complexity remains independent of the bandwidth of excitation. To be more specific, time-periodic EM waves with different bandwidths correspond to the same periodic sequence as long as they have identical waveshape parameters. When integrated with FEM (to handle the spatial part), it provides flexibility and scalability in creating parallel computational algorithms. We will demonstrate the promising potential of TPS by analyzing a broadband transmission case, providing a glimpse into its superior computational efficiency and high accuracy. It is worth mentioning that although this theory is developed in EMs, it also can be applied to other physical subjects such as acoustics, optics, and quantum mechanics.

Table 1 Comparison of TPS and other computational EM algorithms

Algorithm name		Domain category to which the algorithm belongs		
		Continuous transform domain	Discrete time domain	Discrete transform domain
EM signal type suitable for the algorithm	Sinusoid	FD-FEM MoM		FDFD
	Short-time pulse		FDTD	Wavelet
	Long-time pulse			Lagurre
	Periodic arbitrary waveform			TPS

Note: TPS (short for theory of periodic sequence) is a rigorous EM theory designed to process periodic-sequential EM signals with arbitrary waveforms in the discrete transform domain.

II. Theory of Periodic Sequence

In pursuit of our objective, we make use of the method of lines (MoLs), a highly effective half-analytical approach, as introduced in [23]. Typically, MoLs excels in managing the spatial components of PDEs and solving them within specified boundary conditions in specific transform domains. However, in our proposed theory, MoLs take on a novel role by treating and formulating the temporal components of Maxwell's equations under TPBCs. The Maxwell's curl equations will be completely sequentialized and further decoupled in a transform domain by designated mappings. To the best of the authors' knowledge, this represents the first instance of utilizing MoLs to handle temporal parts of PDEs. In subsequent sections of this article, we will show that the transform-domain mappings linked to the temporal case display a stronger constraint in comparison to those associated with the spatial case.

For the sake of formulation, we stipulate that the superscript T represents transpose operator, the superscript † denotes Hermitian operator, the superscript * denotes conjugate operator, and $\lceil\cdot\rceil$ denotes the ceiling truncation. All units are international system of units, and i represents the imaginary unit.

1. Basic theory

In simple and Ohm-lossless media, the Maxwell's curl equations under TPBCs (with time period T) are written as

$$\begin{cases} \nabla\times\boldsymbol{E}(t) = -\mu\dfrac{\partial\boldsymbol{H}(t)}{\partial t} \\ \nabla\times\boldsymbol{H}(t) = +\epsilon\dfrac{\partial\boldsymbol{E}(t)}{\partial t} \end{cases} \tag{1}$$

where ϵ and μ denote the permittivity and permeability, respectively, and

$$\begin{cases} \boldsymbol{E}(t) = \boldsymbol{E}(t+T) \\ \boldsymbol{H}(t) = \boldsymbol{H}(t+T) \end{cases} \tag{2}$$

For simplicity, all the spatial variables are dropped out of (1) and (2).

To achieve a full discretization of the temporal components in (1), all field variables are sampled equidistantly

in the time domain by a leapfrog scheme with time step Δt, as depicted in Figure 1; while their time-partial derivatives are approximated by the first-order difference scheme:

$$\boldsymbol{D}_t = \begin{bmatrix} -1 & 0 & 0 & \dots & 1 \\ 1 & -1 & 0 & \dots & 0 \\ 0 & 1 & -1 & \dots & 0 \\ \vdots & \vdots & \ddots & \ddots & \vdots \\ 0 & 0 & \dots & 1 & -1 \end{bmatrix}_{N\times N} \tag{3}$$

where sequential period is denoted by $N = T/\Delta t$.

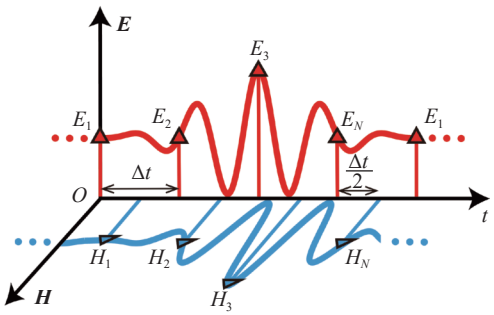

Figure 1 Full time-discretization of Maxwell's curl equations under TPBCs. To simulate discrete EM events, the sampling instant of magnetic field is time-shifted with respect to that of electric field with half-step delay ($\Delta t/2$). The time period T is equidistantly partitioned to N segments, where Δt is subjective to the Nyquist sampling theorem so as to avoid aliasing.

$\boldsymbol{D}_t$ is a circulant matrix, of which the fringe elements are set to characterize the TPBCs. Note that the approximation scheme of time-partial derivative directly decides the numerical accuracy.

Subsequently, the periodic-sequential curl equations can be expressed as

$$\begin{cases} \nabla \times \boldsymbol{E}[n] = \dfrac{\mu}{\Delta t}\boldsymbol{D}_t \boldsymbol{H}[n] \\ \nabla \times \boldsymbol{H}[n] = \dfrac{\epsilon}{\Delta t}\boldsymbol{D}_t^{\mathrm{T}} \boldsymbol{E}[n] \end{cases} \tag{4}$$

Based on (4), the wave equation can be easily derived as

$$\nabla \times \nabla \times \boldsymbol{E}[n] - \frac{\epsilon\mu}{\Delta t^2}\boldsymbol{D}_{tt}\boldsymbol{E}[n] = 0 \tag{5}$$

where

$$\boldsymbol{D}_{tt} = \boldsymbol{D}_t \boldsymbol{D}_t^{\mathrm{T}} = \begin{bmatrix} 2 & -1 & 0 & \dots & 1 \\ -1 & 2 & -1 & \dots & 0 \\ 0 & -1 & 2 & \dots & 0 \\ \vdots & \vdots & \ddots & \ddots & \vdots \\ 1 & 0 & \dots & -1 & 2 \end{bmatrix}_{N\times N} \tag{6}$$

In equation (6), $\boldsymbol{D}_{tt}$ denotes the second-order difference scheme and also possesses circulant elements. In the realm of mathematics, circulant matrices are classified as "normal", implying that they can always undergo diagonalization through unitary matrices. This diagonalization acts as a crucial link between the periodic-sequential domain and the emerging transform domain. It is imperative to observe that these transform operators must adhere to the following stipulated rules:

- The transform operators are able to diagonalize both the first-order (3) and second-order (6) difference schemes.
- Following the application of the inverse mapping, the solution to the wave equation (5) is expected to produce a real number at any given observation point.

Note that the application of MoLs in the spatial domain does not encounter this issue, as the corresponding process initiates with the frequency-domain form of Maxwell's equations.

Consequently, we introduce bilateral mappings $\boldsymbol{T}^{e,h}$ corresponding to the electric/magnetic fields, expressed as follows:

$$\boldsymbol{T}^{e,h} \triangleq \left(\frac{[\mathrm{SGN}(k)]^{n_{e,h}}}{\sqrt{N}} W_N^{-(k-1)(n-\frac{n_{e,h}}{2})} \right)_{nk} \tag{7}$$

where $n = 1,2,\dots,N$, $k = 1,2,\dots,N$, $n_e = 2$ (for electric field), $n_h = 1$ (for magnetic field), $W_N = \exp(\mathrm{i}2\pi/N)$, and $\mathrm{SGN}(k)$ is given by

$$\mathrm{SGN}(k) = \begin{cases} +1, & k = 1,2,\dots,\left\lceil \dfrac{N+1}{2} \right\rceil \\ -1, & k = \left\lceil \dfrac{N+1}{2} \right\rceil + 1, \left\lceil \dfrac{N+1}{2} \right\rceil + 2,\dots,N \end{cases} \tag{8}$$

Note that equation (7) establishes a bilateral mapping or transformation between the periodic-sequential domain and the so-called "w domain" (please refer to Appendix A for a detailed proof).

Utilizing the aforementioned transform mappings on the EM fields within the periodic-sequential domain, we obtain

$$\boldsymbol{e}_k = \boldsymbol{T}^{e^\dagger}\boldsymbol{E}[n] = \frac{1}{\sqrt{N}} \sum_{n=1}^{N} \boldsymbol{E}[n] W_N^{(k-1)(n-1)} \tag{9}$$

and

$$\boldsymbol{h}_k = \boldsymbol{T}^{h^\dagger}\boldsymbol{H}[n] = \frac{\mathrm{SGN}(k)}{\sqrt{N}} \sum_{n=1}^{N} \boldsymbol{H}[n] W_N^{(k-1)(n-\frac{1}{2})} \tag{10}$$

Equations (9) and (10) represent the electric and magnetic field expressions, respectively, in the new transformed domain. To distinguish it from the canonical frequency domain, we name this numerical transform domain as "w domain". Note that for electric field, the transformation is indeed the exact DFT. However, for magnetic field, while the transformation operator remains a unitary matrix, it differs from the canonical DFT in its formulation. In addition to the half-step sampling delay in the discrete-time domain, there is a unique term $\mathrm{SGN}(k)$ present in $\boldsymbol{T}^h$ to ensure that the equations still conform to the law of energy conserva-

tion in the transform domain.

Equation (9)/(10) is conjugate symmetric provided that $\boldsymbol{E}[n]/\boldsymbol{H}[n]$ is real. To be more specific, for each index k, we have

$$\begin{cases} \boldsymbol{e}_{N+2-k} = \boldsymbol{e}_k^* \\ \boldsymbol{h}_{N+2-k} = \boldsymbol{h}_k^* \end{cases} \tag{11}$$

Equation (8) imposes the identical symmetry on both electric field and magnetic field, and it is a compulsory condition, otherwise, the w-domain magnetic field will be conjugate anti-symmetric (due to the delay $\Delta t/2$) and incur non-physical effect which violates the law of energy conservation.

Based on (7), the first- and second-order difference matrices can be diagonalized as

$$\boldsymbol{\Lambda}_k = \boldsymbol{T}^{e\dagger}\boldsymbol{D}_t\boldsymbol{T}^h = 2\mathrm{i}\sin\left[\frac{\pi}{N}(k-1)\right]\mathrm{SGN}(k) \tag{12}$$

and

$$\boldsymbol{\Lambda}_k{}^2 = \boldsymbol{T}^{e\dagger}\boldsymbol{D}_{tt}\boldsymbol{T}^e = -4\sin^2\left[\frac{\pi}{N}(k-1)\right] \tag{13}$$

respectively. Equation (13) implies that $\boldsymbol{D}_{tt}$ has $\lceil (N+1)/2 \rceil$ non-repetitive eigenvalues (denoted by λ_k) due to the symmetric property:

$$\lambda_k = \lambda_{N+2-k}, \quad k = 1, 2, \ldots, k_{\max} \tag{14}$$

where $k_{\max} = \lceil \frac{N+1}{2} \rceil$ denotes the maximum index of the nonzero w-domain components corresponding to the given periodic-sequential excitation. For the sake of comparison, we define the normalized bandwidth (NBW) as

$$\mathrm{NBW} = \frac{2(k_{\max}-1)}{N} \tag{15}$$

We stipulate that the sampling rate of the leapfrog scheme should satisfy $f_s \geq \mathrm{NBW}/\Delta T$ so as to avoid aliasing.

In turn, the w-domain Maxwell's curl equations can be expressed as

$$\begin{cases} \nabla \times \boldsymbol{e}_k = +\mathrm{i}\tilde{\omega}_k \mu\, \boldsymbol{h}_k \\ \nabla \times \boldsymbol{h}_k = -\mathrm{i}\tilde{\omega}_k \epsilon\, \boldsymbol{e}_k \end{cases} \tag{16}$$

where

$$\tilde{\omega}_k = \frac{2}{\Delta t}\sin\left[\frac{\pi}{N}(k-1)\right]\mathrm{SGN}(k) \tag{17}$$

$\tilde{\omega}_k$ possesses the conjugate anti-symmetric property, i.e., $\tilde{\omega}_k = -\tilde{\omega}_{N+2-k}$. This anti-symmetry leads to real sequential response after inversely mapping the solutions of (16) to the periodic-sequential domain.

Equation (17) can be further rewritten as

$$\tilde{\omega}_k = \omega_k\, \mathrm{Sa}\left[\frac{\pi}{N}(k-1)\right], \quad k = 1, 2, \ldots, \left\lceil \frac{N+1}{2} \right\rceil \tag{18}$$

where

$$\omega_k = 2\pi f_k = \frac{2\pi(k-1)}{T} \tag{19}$$

ω_k and f_k denote the circular frequency and frequency corresponding to the k-th index, respectively, and the factor $\mathrm{Sa}[\pi(k-1)/N]$ depicts the numerical approximation which is related to not only the sequential period N but also the spectrum index k. As N tends towards infinity and with a fixed value of k, the quantized spectrum $\tilde{\omega}_k$ approaches the circular frequency ω_k.

Substituting $k = N+2-k$ to (16), we have

$$\begin{cases} \nabla \times \boldsymbol{e}_{N+2-k} = +\mathrm{i}\tilde{\omega}_{N+2-k}\ \mu\, \boldsymbol{h}_{N+2-k} \\ \nabla \times \boldsymbol{h}_{N+2-k} = -\mathrm{i}\tilde{\omega}_{N+2-k}\ \epsilon\, \boldsymbol{e}_{N+2-k} \end{cases} \\ \Downarrow \\ \begin{cases} \nabla \times \boldsymbol{e}^*_{N+2-k} = +\mathrm{i}\tilde{\omega}_k \mu\, \boldsymbol{h}^*_{N+2-k} \\ \nabla \times \boldsymbol{h}^*_{N+2-k} = -\mathrm{i}\tilde{\omega}_k \epsilon\, \boldsymbol{e}^*_{N+2-k} \end{cases} \tag{20}$$

Comparing (20) with (16), it is obvious to see that the anti-symmetric property of $\tilde{\omega}_k$ ensures the conjugate symmetry of the solution of w-domain curl equations. Once mapping the fields back to the original domain, they stay real as required.

We should note that the theory discussed above can be easily extended to the Ohm-lossy case, allowing us to further derive the law of energy conservation in the w domain. For more details, please refer to Appendix B.

2. Quantized spectrum vs. circular frequency

The difference scheme plays a crucial role in the development of TPS. While the first-order difference scheme (3) offers a succinct analysis for establishing the basics of TPS, it is accompanied by incidental numerical losses. Therefore, it becomes imperative to scrutinize this deviation in order to enhance numerical accuracy.

The discrepancy between $\tilde{\omega}_k$ and ω_k is due to the approximation of the time-partial derivative through difference schemes. Therefore, it is important to carefully select a difference scheme as it directly impacts the numerical accuracy. Fortunately, by introducing the recurrent difference scheme [24], we can improve the accuracy without changing the transform operators (7).

According to Taylor series expansion, the first-order difference scheme can be expressed as

$$\frac{\psi_{i+1} - \psi_i}{2} = \left[\frac{\frac{\Delta t}{2}}{1!}\frac{\partial}{\partial t} + \frac{\left(\frac{\Delta t}{2}\right)^3}{3!}\frac{\partial^3}{\partial t^3} + \frac{\left(\frac{\Delta t}{2}\right)^5}{5!}\frac{\partial^5}{\partial t^5} + \cdots\right]\psi \tag{21}$$

Based on (21), we can build up the recurrent difference scheme as follows:

$$\frac{\partial}{\partial t} = \frac{D}{\Delta t}\left\{1 + \frac{\left(\frac{\Delta t}{2}\right)^2}{3!}\frac{\partial^2}{\partial t^2}\left[1 + \frac{3!\left(\frac{\Delta t}{2}\right)^2}{5!}\frac{\partial^2}{\partial t^2}(1+\cdots)\right]\right\}^{-1} \tag{22}$$

where D represents the first-order difference scheme $\{-1, 1\}$. Note that the first-order difference scheme is explicit while the expression of recurrent difference operator is implicit. Subsequently, we use the former one to establish our theoretical model and take the later one for practical computation. Inserting (6) to (22), In the w domain, we have

$$\tilde{\omega}_k^{(1)} = \frac{\tilde{\omega}_k}{\mathrm{sinc}(\tilde{\omega}_k/2)} \tag{23}$$

If we denote $\tilde{\omega}_k$ as $\tilde{\omega}_k^{(0)}$, the quantized spectrum after q times of recurrence can be expressed as

$$\tilde{\omega}_k^{(q)} = \frac{\tilde{\omega}_k^{(0)}}{\mathrm{sinc}(\tilde{\omega}_k^{(q-1)}/2)} \tag{24}$$

Obviously, given $q \to \infty$, ω_k is the limitation of $\tilde{\omega}_k^{(q)}$. Figure 2 illustrates the normalized magnitude of $\tilde{\omega}_k$ in comparison to ω_k across various orders of recurrence. It is evident that the relative error becomes prominent as $k_{\max}$ attains larger values. In other words, a longer "close-to-unity" span corresponds to improved accuracy performance of a difference scheme. Depending on the bandwidth of a given periodic sequence, distinct orders of recurrence are required. With a sufficiently large N, achieving this with a lower order of recurrence becomes feasible.

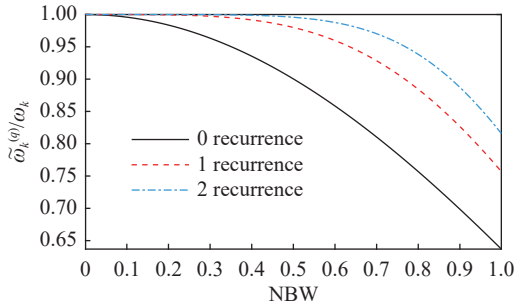

Figure 2 Normalized quantized spectrum $\tilde{\omega}_k^{(q)}/\omega_k$ as a function of NBW across various orders of recurrent difference schemes. With a constant length of N, the region approaching unity experiences a notable expansion as the recurrent order q increases.

Furthermore, the numerical dispersion is related to both time and spacial discretizations. In order to analyze their effects on the dispersion, we investigate the dispersion relation in two-dimensional (2D)-problem space. Assuming that an infinite plane is filled with lossless, isotropic, and homogeneous media, then a w-domain plane wave can be defined as

$$e_k = \exp[\mathrm{i}(\kappa_x x + \kappa_y y)] \tag{25}$$

Partitioning the plane by triangular mesh, we insert (25) to (16) and replacing the infinite boundary condition with the Floquet periodic boundary condition [25], we can derive the dispersion relation as equation (26).

$$\begin{aligned}\kappa_{k_{\max}}{}^2 = {} & \kappa_x{}^2 + \kappa_y{}^2 + \frac{\pi^4 \epsilon\mu}{12\Delta t^2}\mathrm{NBW}^4 + (\alpha\kappa_1{}^4 + \beta\kappa_x{}^3\kappa_y \\ & + \gamma\kappa_x{}^2\kappa_y{}^2 + \delta\kappa_x\kappa_y{}^3 + \theta\kappa_y{}^4) + O(\kappa^4)\end{aligned} \tag{26}$$

where O represents the higher-order infinitesimal and the w-domain wavenumber κ_k is given by

$$\kappa_k = -\kappa_{N+2-k} = \tilde{\omega}_k\sqrt{\epsilon\mu}, \quad k = 1, 2, \ldots, \left\lceil \frac{N+1}{2} \right\rceil \tag{27}$$

α, β, γ, δ, and θ represent the geometric coefficients which are decided by the given type of edge element. Note that κ_k keeps non-negative within the first half of the quantized spectrum. In turn, it allows us to use the sign ahead of κ_k to discern the direction of propagation.

Equation (26) indicates that the 4-th-order numerical error is composed of the items corresponding to both time and spatial discretization. Generally speaking, the spatial discretization can be deemed as a minor contributor given an appropriate mesh (not too coarse). Note that the contribution of spatial discretization will reduce to the 6-th-order if the grid is constituted by equilateral triangles. In order to assess the dispersion level, we define the relative error of propagation constant as

$$p = \frac{|\kappa_{k_{\max}} - \omega_{k_{\max}}\sqrt{\epsilon\mu}|}{\omega_{k_{\max}}\sqrt{\epsilon\mu}} \times 100\% \tag{28}$$

For illustration, we test the relative error of rectangular waveguide (RWG) under perfect electrical conductor (PEC) condition (see Appendix C for more details), which also has an analytical solution in the w domain. Assuming that waveguide is infinitely long in $\hat{z}$ direction (lateral dimension $a \times b$), the wave equation can be expressed as

$$\begin{cases} \nabla^2 \boldsymbol{e}_k + \kappa_k^2 \boldsymbol{e}_k = 0 \\ \nabla^2 \boldsymbol{h}_k + \kappa_k^2 \boldsymbol{h}_k = 0 \end{cases} \tag{29}$$

In turn, it allows us to use the sign ahead of κ_k to discriminate the propagating direction.

As a consequence, the w-domain dispersion of the RWG can be derived as

$$\kappa_{z_k} = \sqrt{\kappa_k{}^2 - \left(\frac{m\pi}{a}\right)^2 - \left(\frac{l\pi}{b}\right)^2} \tag{30}$$

where a and b represent the width and height of RWG, respectively, and (m, l) stands for the spatial-modal index pair. Since equation (30) is related to the index k, we stipulate that the complete set of $\{\mathrm{TE}_{10k}\}$ $(k = 1, 2, \ldots, k_{\max})$ represents the "TE_{10} mode" of RWG (please refer to Appendix D for detail on the TE_{mlk} mode of RWG).

Figures 3(a)–(c) illustrate the relative error of propagation constant of a WR-284 RWG, corresponding to different recurrent orders. It is clearly to see that the numerical curves are fitting well with those analytical ones, indicating that the numerical dispersion will dominate the dispersion relation (26) under an appropriate mesh. If κ_{z_k} is much big-

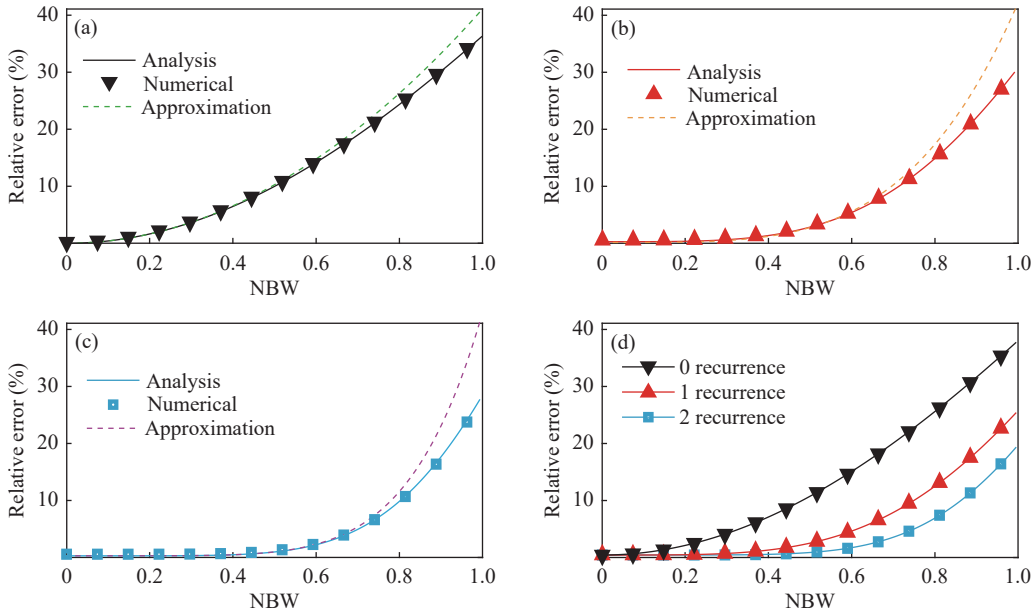

Figure 3 Relative error of propagation constant p: $TE_{10k_{max}}$ mode of WR-284 (lateral dimension: 72.136 mm × 34.036 mm). (a) Difference scheme without recurrence. (b) 1st-recurrent difference operator. (c) 2nd-recurrent difference operator. (d) Relative error p vs. recurrence order. Here, "Analysis" (solid) denotes the analytical dispersion relation of $TE_{10k_{max}}$ mode (30); "Numerical' (curve with marker) represents the result derived from 2D FEM, and "Approximation" (dash) corresponds to the empirical formulas (31)–(33).

ger than the third item on the right side of (26), then (28) can be approximated as

$$p = \frac{\pi^2}{24}\mathrm{NBW}^2 \tag{31}$$

As shown in Figure 3(a), equation (31) keeps a good consistency with the theoretical result within a considerable span of NBW. Also, it indicates that the numerical dispersion is proportional to the power of NBW, so we can suppress the dispersion by brutally increasing the periodic length N. However, this might require a large N to achieve a satisfied accuracy. Fortunately, the recurrent spectrum (24) can greatly alleviate this problem. Figures 3(b) and (c) illustrate the cases of first- and second-order recurrence, the corresponding approximations of (28) can be expressed as

$$p = \frac{\pi^4}{288}\mathrm{NBW}^4 \tag{32}$$

and

$$p = \frac{\pi^6}{3456}\mathrm{NBW}^6 \tag{33}$$

respectively. Given a fixed accuracy level, the qualified span of NBW is extended with the increase of recurrent order, as shown in Figure 3(d), leading to a well-restrained dispersion level.

3. Periodic-sequential excitation and general computational process

Contrasting with conventional frequency-domain analysis, often tied to sinusoids (single-point spectrum), periodic sequential excitation assumes a pivotal role in TPS, making a substantial contribution by carrying richer signal information within its waveform. In the w domain, the computational scale depends on the maximum index $k_{\max}$ of a given excitation. The general process of obtaining $k_{\max}$ is listed as follows:

1) Setting waveshape parameters of a specific waveform in the continuous-time domain, such as (root) raised-cosine, trapezoidal, and Gaussian waveforms.

2) Cutting off the corresponding spectrum in the continuous-frequency domain, denoted by f_c.

3) Deriving $k_{\max}$ numerically by solving the optimization problem $\arg\min_k\{\tilde{\omega}_k^{(q)} - 2\pi f_c\}$ subject to $\tilde{\omega}_k^{(q)} \le 2\pi f_c$.

For the sake of analysis, we equidistantly divide period T to K segments, i.e., $T = KT_s$, where $T_s = N_s\Delta t$. As a result, we have $N = KN_s$. Correspondingly, N can be equidistantly partitioned to K segments, i.e., $N = KN_s$ where N_s denotes the code duration or unit interval (UI).

In turn, the above optimization problem is equivalent to

$$\arg\min_k \left\{ \frac{N_s \sin\left[\dfrac{\pi(k-1)}{N}\right]}{\pi \mathrm{sinc}\left(\dfrac{\tilde{\omega}_k^{(q-1)}}{2}\right)} - \frac{f_c}{F_s} \right\} \tag{34}$$

subject to

$$\frac{N_s \sin\left[\dfrac{\pi}{N}(k-1)\right]}{\pi \mathrm{sinc}\left(\dfrac{\tilde{\omega}_k^{(q-1)}}{2}\right)} \le \frac{f_c}{F_s} \tag{35}$$

where $F_s = 1/T_s$.

Note that item f_c/F_s in (34) are dimensionless, so $k_{\max}$ is not related to the bandwidth of original signals. This means that time-periodic EM waves with different bandwidths correspond to the same periodic sequence as long as they have identical waveshape parameters. Consequently, given a fixed UI-measured period K, we can arbitrarily compress the original transient pulse while still preserving the same computational scale in the w domain, as illustrated in Figure 4.

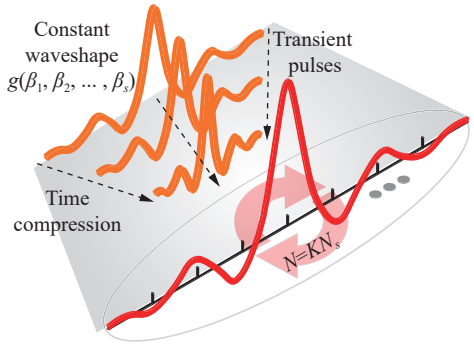

Figure 4 General process of periodic sequential excitation. The computational scale in the w domain is independent of the bandwidth of the original transient pulse, offering a promising computational advantage in the broadband transmission scenario.

Moreover, considering the ideal scenario that $q \to \infty$, then $k_{\max}$ can be explicitly expressed as

$$k_{\max} = \left\lfloor \left(\frac{f_c}{F_s} \right) K \right\rfloor \tag{36}$$

where $\lfloor \cdot \rfloor$ denotes the floor-integer operator. Since f_c/F_s is only decided by time-domain waveshape parameters and transform-domain cut-off criterion, we rewrite (36) to

$$k_{\max} = \lfloor g(\beta_1, \beta_2, \ldots, \beta_S) K \rfloor \tag{37}$$

where $g(\cdot)$ is the function of waveshape and cut-off parameters $\{\beta_s\}_{s=1}^{S}$. A different waveform will result in a different scale of computation.

As depicted in Figure 5, the expressions of $g(\cdot)$ which correspond to raised-cosine, trapezoidal, and Gaussian periodic sequences are

$$g(\alpha) = \frac{1+\alpha}{2} \tag{38}$$

$$g(r) = \frac{1}{r} \tag{39}$$

and

$$g(t_p, f_p) = \frac{2}{\pi} \sqrt{\ln(t_p) \ln(f_p)} \tag{40}$$

respectively.

For raised-cosine case (38), α denotes the roll-off factor, within the range $[0, 1]$. For trapezoidal case (39), r represents the rise-time ratio. For Gaussian case (40), t_p and f_p

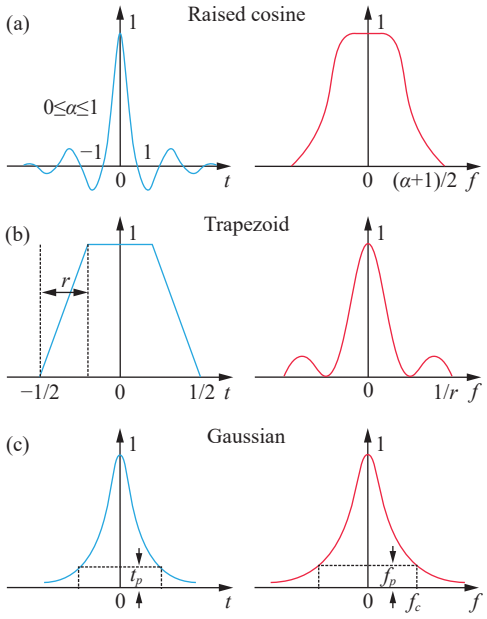

Figure 5 Waveform parameter and cut-off criterion of commonly used periodic sequences.

depict the truncation positions in time and transform domain, respectively. Alternatively, we use time-bandwidth product BT instead of t_p as the waveshape parameter, and their relation is shown as follows:

$$t_p = \exp\left[-\left(\pi BT / \sqrt{2\ln 2} \right)^2 \right] \tag{41}$$

It is clearly to see that once a specific waveform is selected, the computational scale only depends on the UI-measured period K. Hence, if K is appropriately sized, there is a significant promise for rapidly solving Maxwell's equations in the w domain via parallel computation.

As illustration, we have investigated the propagation of a modulated-Gaussian periodic sequence in a standard WR-10 RWG (2.54 mm × 1.27 mm × 50.00 mm). The bandwidth of the baseband Gaussian equals to 17.5 GHz and the carrier frequency is set to 97.5 GHz. The waveshape parameters (t_p, f_p) are set to $(0.01, 0.01)$. To explore the impact of varying recurrent orders in the difference scheme, the parameters N_s and K are fixed at 50 and 5, respectively.

The overall parallel scale in the w domain is set to 10. Figure 6(a) illustrates the input modulated-Gaussian periodic sequences under different recurrent orders, showcasing identical waveforms. However, significant spectral differences emerge between the spectrum corresponding to the first-order difference scheme and the first- and second-order recurrent schemes, as depicted in Figure 6(b). The deviation in the quantized spectrum reflects the numerical errors induced by difference schemes, and this deviation enlarges with the increasing index k. Figure 6(c) displays the corresponding output response of RWG. Notably, in the case of a large NBW, the first-order difference scheme leads to considerable numerical dispersion. Therefore, to ensure robust

numerical accuracy, we opt for the second-order recurrent difference scheme in practical applications.

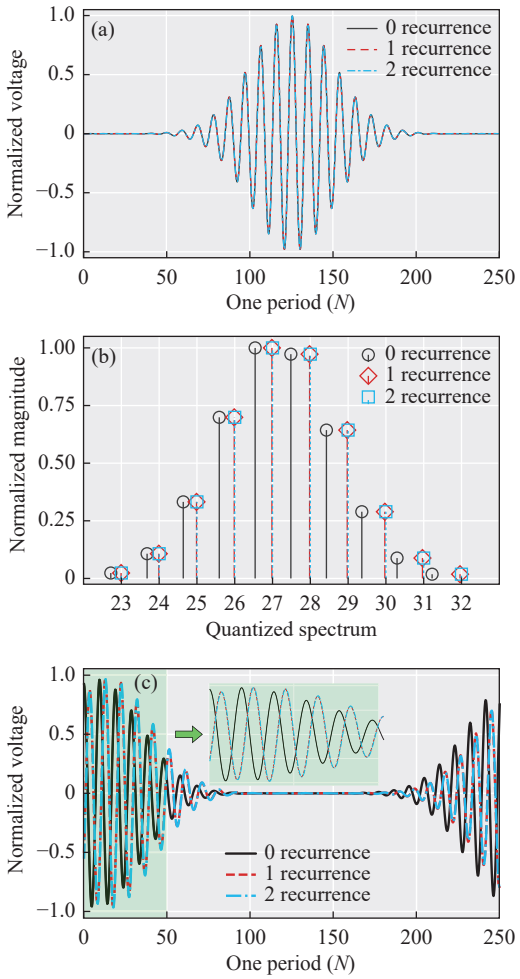

Figure 6 Propagation of modulated-Gaussian periodic sequence in RWG. (a) Input modulated-Gaussian periodic sequence vs. recurrent orders of difference scheme. (b) Corresponding quantized spectrum. (c) Periodic sequential responses of WR-10 (2.54 mm ×1.27 mm × 50.00 mm).

The aforementioned theory only involves the temporal part of Maxwell's curl equations—we must introduce spatial-part process in the w domain so as to solve general EM problems. Without loss of generality, FEM is chosen as the w-domain solver, in which EM fields are represented by the first-type Nédélec edge elements [26]. In this article, we focus on the the close-region scenario and electrical excitation.

The general process of w-domain parallel computation is straightforward, as illustrated in Figure 7. First, the periodic-sequential excitation is mapped to the w domain by FFT. By inspecting its quantized spectrum, one can easily get the maximum index which decides the computational scale. For each index k, an FEM solver will be called to yield the corresponding output. Due to the parallel nature of TPS, it is very promising to implement multiprocessing to solve those subroutines independently. After all the subroutines are completed, the outcomes will be synthesized and inversely mapped to the periodic-sequential domain via IFFT. The output is still a periodic sequence and can be deemed as the "system response" of the entire problem space.

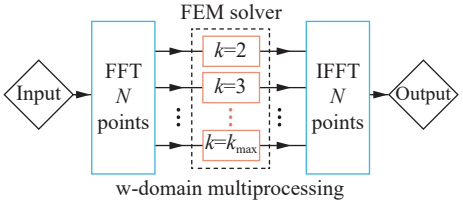

Figure 7 General process of w-domain parallel computation. The computational scale is decided by $k_{\max}$. Multiprocessing technique is adopted in w domain so as to solve each componential equation.

Assuming that the close-region problem only involves two types of boundary conditions: "PEC" and "waveport". For each w-domain index, the matrices equation can be expressed as [17]

$$\left\{\boldsymbol{P}^e-\kappa_k^2\boldsymbol{Q}^e+\mathrm{i}\tilde{\omega}_k\mu_0\sum_{p=1}^{P}\sum_{m=1}^{\infty}\boldsymbol{b}_{mk}^p\boldsymbol{b}_{mk}^{p\,\mathrm{T}}\right\}\boldsymbol{e}_k=2\mathrm{i}\tilde{\omega}_k\mu_0\sum_{p=1}^{P}\sum_{m=1}^{\infty}\boldsymbol{b}_{mk}^p \tag{42}$$

where

$$\begin{aligned}\boldsymbol{P}_{ij}^e&=\iiint_{V_e}(\nabla\times\boldsymbol{N}_i^e\cdot\bar{\mu}^{-1}\cdot\nabla\times\boldsymbol{N}_j^e)\mathrm{d}V\\ \boldsymbol{Q}_{ij}^e&=\iiint_{V_e}(\boldsymbol{N}_i^e\cdot\bar{\epsilon}\cdot\boldsymbol{N}_j^e)\mathrm{d}V\\ (\boldsymbol{b}_{mk}^{\mathrm{p}})_i&=\iint_{S_e^p}(\boldsymbol{N}_i^e\times\boldsymbol{h}_{mk}^p)\cdot\hat{n}\mathrm{d}S\end{aligned} \tag{43}$$

where μ_0 denotes the vacuum permeability; $\bar{\epsilon}$ and $\bar{\mu}$ are the tensor form of relative permittivity and permeability, respectively; $\boldsymbol{N}_{i,j}^e$ represents the vector finite element basis of the tetrahedral (triangular) element $V_e(S_e^p)$; the subscripts i and j denote the global index of the vector basis; $\boldsymbol{h}_{mk}^p$ is the normalized magnetic modal field; the superscripts p and m denote the p-th port (P ports total) and the spatial index of the modal field, respectively. Similar to traditional frequency domain, we extend the concept of scattering parameters (S-parameters) to the w domain, referred to as quantized S-parameters as follows:

$$s_{mk}^{pp_0}=\boldsymbol{b}_{mk}^{p\,\mathrm{T}}\boldsymbol{e}_k-\delta_{pp_0} \tag{44}$$

Here, the excitation is only assigned to the p_0-th port. If $p=p_0$, δ_{pp_0} equals to one otherwise zero. Besides, the eigenvalue problem on each port surface is solved by modifying (27) in [27]. The corresponding process is similar to (42), hence the details are omitted here due to space limitation.

Once the quantized S-parameters have been obtained, it is easily to derive the output response for arbitrary port. The overall process can be summarized as

$$\tilde{q}[n]=\tilde{h}[n]\overset{N}{\circledast}\tilde{p}[n] \tag{45}$$

where $\tilde{p}[n]$, $\tilde{h}[n]$, and $\tilde{q}[n]$ represent the input excitation, the "impulse response" of the close-region, and the corresponding "system response", respectively; the tilde sign indicates that the sequence is periodic type and $\overset{N}{\circledast}$ represents the N-points circular convolution. Note that the response is only related to the sequence —all spatial variables have been eliminated via the surface integration on each port.

Equation (45) bridges the gap between the "IFFT operation on the excitation" and the "IFFT operation on the response". In fact, the formulation associated with TPS determines the "system response". The "system response" is dictated by the formulation associated with TPS. In essence, the procedures carried out by researchers and engineers closely resemble the limiting case where the ∞-order recurrent operator is applied, leading to $\tilde{\omega}_k^{(\infty)} = \omega_k$.

III. Experimental Demonstration

As mentioned earlier, time-periodic waves with arbitrary waveforms are able to convey more valuable signal information than sinusoids. This category of EM waves holds potential applications in the analysis of broadband transmission and the design of high-speed RF devices. Hence, it is meaningful to explore their propagation behavior in practical scenarios. In this section, we undertake two experimental measurements related to time-periodic waves with assigned waveforms and investigate whether TPS can provide an accurate analysis for the propagation of those time-periodic EM waves.

1. Propagation of periodic-sequential wave in RWG

As mentioned earlier, RWG can be characterized by analytical expressions that correspond to EM fields in the w domain. Consequently, we selected a standard RWG as our first benchmark to validate the proposed theory. For testing purposes, we utilized the Keysight M8190A arbitrary waveform generator (AWG) with a maximum sampling rate of 12 GSa/s. The chosen device under test (DUT) is a standard RWG with the designation WR-284. The physical dimension of WR-284 is 72.14 mm × 34.04 mm × 420 mm, and its TE_{10}-mode cutoff frequency is approximately 2.08 GHz. The selection of WR-284 as the DUT aligns with the constraints imposed by the maximum sampling rate of the Keysight M8190A AWG, ensuring compatibility and accuracy in our experimental setup.

Figure 8(a) depicts the measurement setup. The primary channel comprises a Keysight M8190A, a real-time oscilloscope (OSC) Agilent Infiniium DSO81204B (with a maximum sampling rate of 40 GSa/s), and the DUT RWG, along with fixtures and coaxial cables. The secondary channel facilitates a direct connection between the AWG and the OSC, linked by cables of identical length to those in the primary channel. By considering the second channel as the reference, any delay introduced by the cables in the first channel can be easily eliminated.

Figures 8(b) and (c) illustrate the input modulated-Gaussian periodic sequence and its quantized spectrum, respectively. Due to the high-pass property of RWG, we can choose a modulated periodic Gaussian sequence as the excitation. The waveshape parameters (t_p, f_p) are set to (0.01, 0.10) with $N_s = 729$ and $K = 3$. The corresponding data rate and carrier frequency are fixed at 1.5 GHz and 2.5 GHz, respectively.

Figure 8(d) illustrates the output sequence derived from the OSC and that predicted by our proposed method. For the sake of comparison, the magnitude is normalized in both cases. It is evident that the theoretical curve closely matches the experimental curve. Due to the limited maximum sampling rate of the AWG, there is a slight distortion in the experimental results. Nevertheless, these experimental findings provide substantial support for the validity of our proposed theory.

As aforementioned in Section II.3, TPS exhibits inherent computational advantages in the scenario of broadband EM transmission. To substantiate this advantageous feature, we designed and manufactured four high-speed boards with varying routine delays, denoted as cases 1–4, as illustrated in Figures 9(d)–(g). The microstrip boards under test are constructed from Rogers RO3003 substrate with a thickness of 5 mil, and they operate in the frequency range from direct current (DC) to 50 GHz. Both routines, each with a width of 0.3 mm, are terminated by V-band end launchers. To investigate the crosstalk effects, we set the coupling length and gap spacing to 10.0 mm and 0.2 mm, respectively, ensuring a significant coupling effect. The difference in length between routine port 1–port 2 ("long") and routine port 3–port 4 ("short") is equal to 1/3/5/7 mm.

2. Broadband transmission

Figure 9(a) shows the setup of the experimental system. It is composed of an AWG Keysight M8196A (maximum sampling rate at 92 GSa/s), the DUT crosstalk boards, a real-time OSC UXR0702AP (maximum sampling rate at 256 GSa/s) and four V-band cables. The outputs of AWG are controlled by the panel of Keysight IQtools. To avoid aliasing, the sampling rate of AWG is set to 90 GSa/s. After the in-system calibration, the AWG channels are synchronized (the skew is less than 0.2 ps), and the attenuation is considerably alleviated. The loss, delay, and inter-channel skew of the V-band cables are removed by the common procedure of the in-system calibration and the Keysight D9020ASIA advanced signal integrity (SI) software.

To provide a reasonable comparison between simulation and measurement, we send a raised-cosine ($\alpha = 1$) broadband pulse (with bandwidth 45 GHz) to AWG, and take the average of output (4096 waveforms) as the excitation. The discrepancy between the two synchronized AWG outputs and the ideal reference can be easily observed from Figures 9(b)–9(c). Since $k_{\max} = 10$ corresponds to a small computational scale, we implement one-batch multiprocessing to solve those components simultaneously.

For a quantitative comparison of output system responses (denoted by $\widetilde{q}_1[n]$ and $\widetilde{q}_1[n]$, respectively), we utilize the Kullback-Leibler (KL) divergence as the figure of

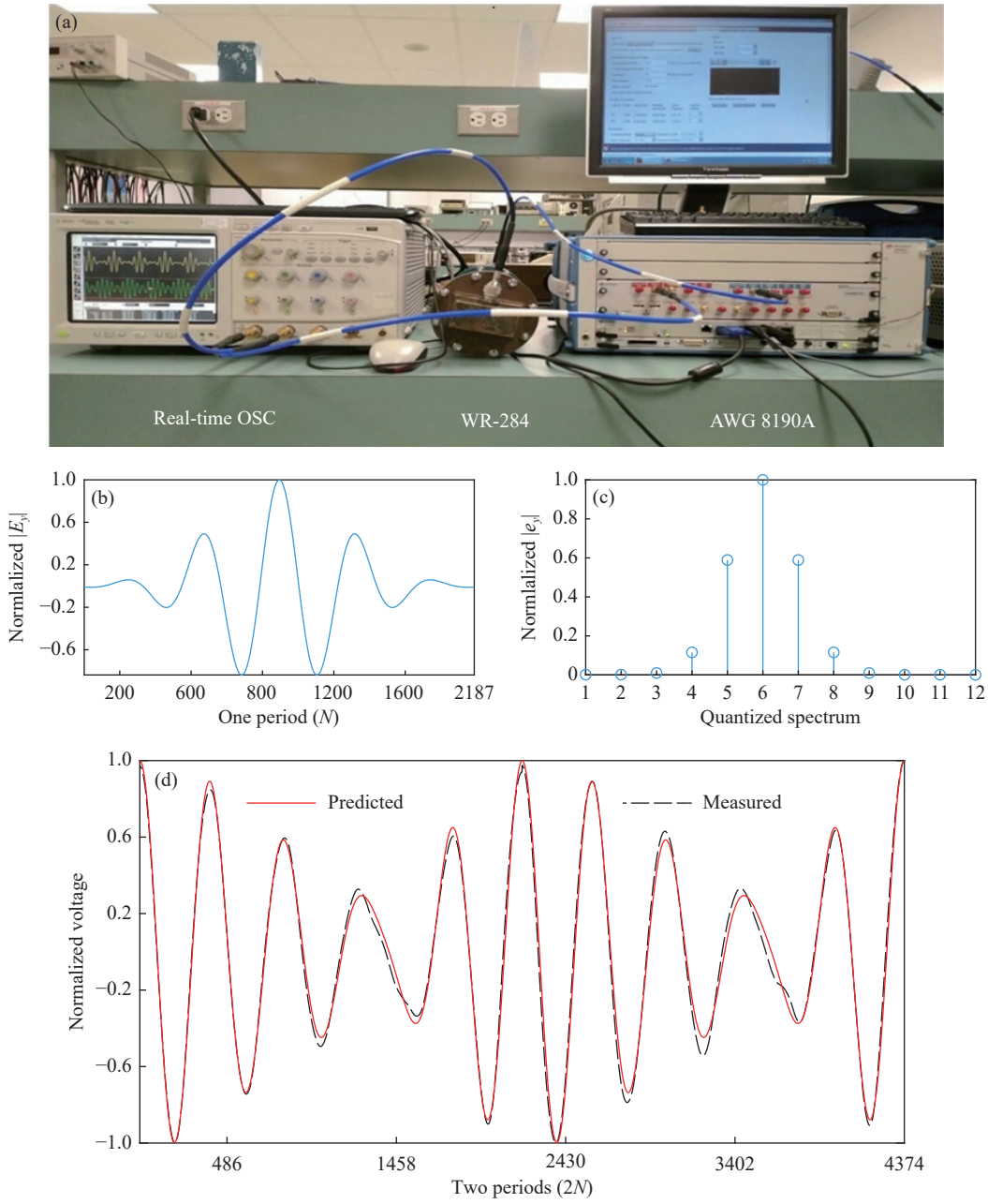

Figure 8 Experimental validation 1: periodic-sequential EM wave propagating in RWG. (a) Photo of validation system. (b) Input modulated-Gaussian periodic sequence. (c) Corresponding w-domain quantized spectrum. (d) Periodic system responses—prediction vs. measurement.

merit to assess the performance of our proposed method in comparison to the measured benchmark. In mathematics, the KL divergence is a measure of deviation between two non-negative vectors[28]:

$$D_{\mathrm{KL}}(u,v)=\sum_{n=1}^{N}\left\{u[n]\ln\frac{u[n]}{v[n]}-u[n]+v[n]\right\} \tag{46}$$

where $u[n]=|\widetilde{q}_1[n]|/\|\widetilde{q}_2[n]\|_2$, $v[n]=|\widetilde{q}_2[n]|/\|\widetilde{q}_2[n]\|_2+\varepsilon$, and $\varepsilon=10^{-12}$. The error ε is to ensure that each component of v is positive. Note that the bounds of sum and norm in (46) are both limited within one sequential period. It is clear to see that KL divergence is non-negative and equals to zero if and only if two sequences are identical, i.e. $u=v$. Generally speaking, $D_{\mathrm{KL}}(u,v)$ does not equal to $D_{\mathrm{KL}}(v,u)$. Hence, we stipulate that the second sequence (corresponding to measurement) is always deemed as the reference.

Figures 9(d)–(g) illustrate the periodic responses of the under-tested circuits (cases 1–4) according to the prediction and the measurement, respectively. The effects of far-end crosstalk (FEXT) are captured in both the simulation and measurement. In each case, the predicted curves are fitting well with the measured ones, and this observation is further corroborated by the corresponding small KL divergences.

As demonstrated by these experiments, we can con-

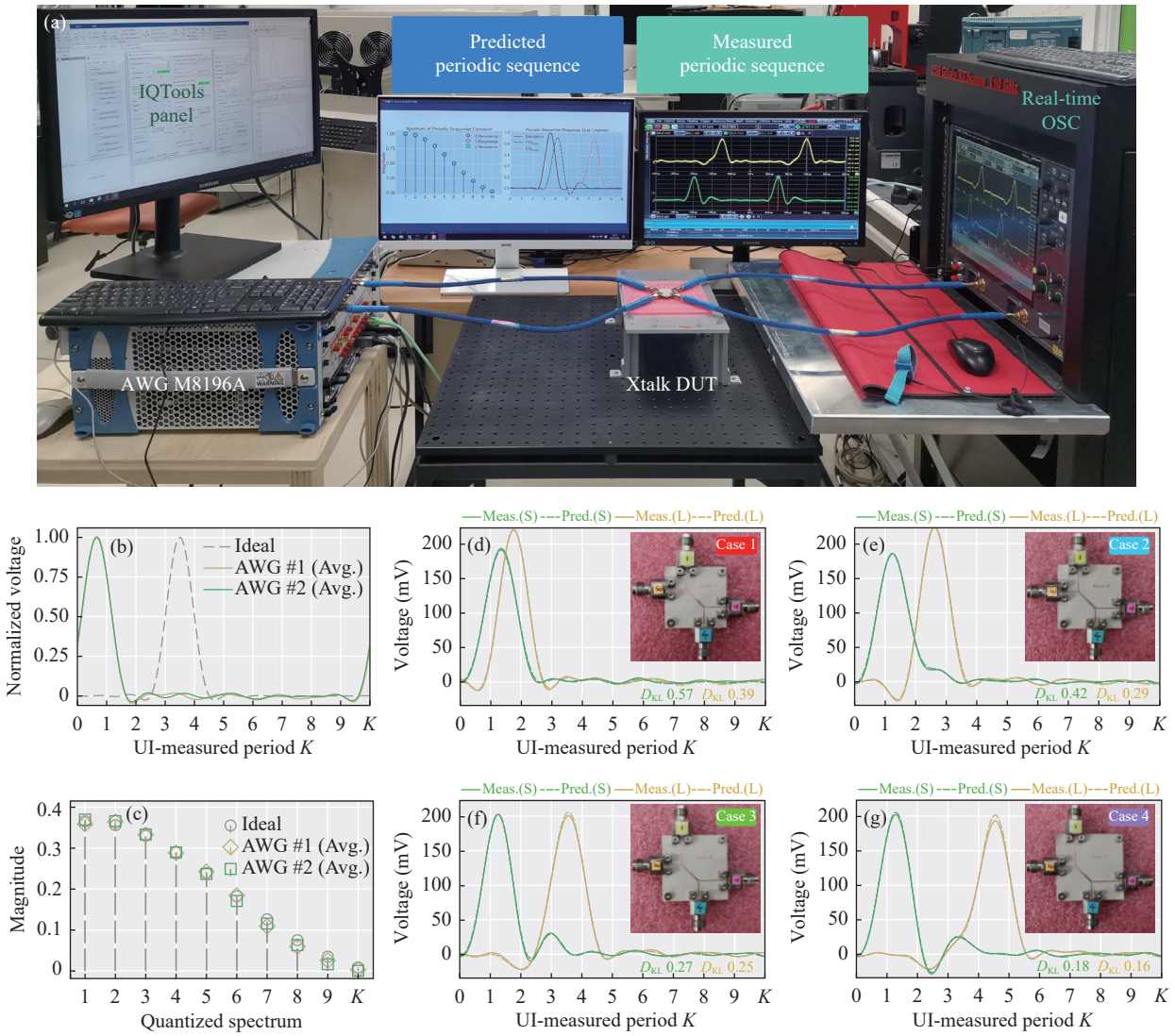

Figure 9 Coupling between EM periodic sequences according to 45 GHz-broadband pulse. (a) Photo of measurement setup. (b) and (c) Input periodic raised-cosine sequences and the corresponding spectrum—ideal (gray dashed), the outputs of AWG channel 1 (golden solid) and channel 2 (green solid), as the average results of consecutive 4096 waveforms. (d)–(g) Average periodic responses of the under-tested circuits (cases 1–4): algorithm predictions vs. measured results.

clude that TPS indeed possesses the capability to provide an accurate simulation, executed through parallel computation, to depict the propagation of continuous time-periodic EM waves with diverse waveforms across different wavelength scales. It should be noted that TPS is better suited for handling (ultra-)wideband scenarios without sharp resonant peaks in the spectrum. If the resonant peaks are distributed over a wide spectral span, this may result in significant computational overhead.

IV. Conclusion

In summary, we have presented, to the best of our knowledge, the first open publication and development on TPS and its applications concerning time-periodic EM waves. TPS demonstrates its effectiveness in successfully depicting the propagation process of EM periodic sequences with arbitrary waveforms. The accuracy of the proposed theory and method is substantiated by experimental measurements of time-periodic waves with assigned waveforms. It is important to note that, in reality, Maxwell's equations and EM signals are continuous in the time domain. Therefore, the application of TPS is accurate only when signals are truly periodic or can be approximated as such in both time and frequency domains. The bandwidth-independent property of periodic sequences and the parallel nature of the w-domain Maxwell's equations make TPS a potential tool for the analysis of (ultra-)wideband wired/wireless channels and facilitate the rapid design of high-speed RF devices in the future.

Appendix A. Existence Proof of $T^{e,h}$

Theorem A-1 Fourier transform of a discrete-time sequence exists if and only if the sequence is summable.

Proof Regarding the electric field, T^e is essentially a DFT operator,

and therefore the corresponding proof is omitted.

In the case of the magnetic field, $\boldsymbol{h}_k$ exists if $\boldsymbol{H}[n]$ is absolutely summable. This can be easily proved as follows:

$$\begin{aligned}|\boldsymbol{h}_k| &= |\boldsymbol{T}^{h^\dagger}\boldsymbol{H}[n]| = \frac{1}{\sqrt{N}}\left|\sum_{n=1}^{N}\boldsymbol{H}[n]\mathrm{SGN}(k)W_N^{-(k-1)(n-\frac{1}{2})}\right| \\ &\le \frac{1}{\sqrt{N}}\sum_{n=1}^{N}|\boldsymbol{H}[n]\mathrm{SGN}(k)W_N^{-(k-1)(n-\frac{1}{2})}| \\ &= \frac{1}{\sqrt{N}}\sum_{n=1}^{N}|\boldsymbol{H}[n]|\cdot|\mathrm{SGN}(k)W_N^{-(k-1)(n-\frac{1}{2})}| \\ &\le \frac{1}{\sqrt{N}}\sum_{n=1}^{N}|\boldsymbol{H}[n]| < \infty \end{aligned} \tag{A-1}$$

Appendix B. Ohm-Lossy Scenario and Energy Conservation

In Ohm-lossy scenario, the periodic-sequential curl equations can be written as

$$\begin{cases}\nabla\times\boldsymbol{E}_n = \dfrac{\mu}{\Delta t}\boldsymbol{D}_t\boldsymbol{H}_n \\ \nabla\times\boldsymbol{H}_n = \left(\sigma\boldsymbol{O} + \dfrac{\epsilon}{\Delta t}\boldsymbol{D}_t\right)^{\mathrm{T}}\boldsymbol{E}_n\end{cases} \tag{B-1}$$

where σ denotes the conductivity of the lossy material and the averaging operator $\boldsymbol{O}$ is defined as

$$\boldsymbol{O} = \frac{1}{2}\begin{bmatrix}1 & 0 & 0 & \dots & 1\\ 1 & 1 & 0 & \dots & 0\\ 0 & 1 & 1 & \dots & 0\\ \vdots & \vdots & \ddots & \ddots & \vdots\\ 0 & 0 & \dots & 1 & 1\end{bmatrix}_{N\times N} \tag{B-2}$$

Note that the sample timing of electric field is identical to that of magnetic field in the second equation of (B-1). In the w domain, we have

$$\begin{cases}\nabla\times\boldsymbol{e}_k = +\mathrm{i}\tilde{\omega}_k\mu\,\boldsymbol{h}_k \\ \nabla\times\boldsymbol{h}_k = (o_k - \mathrm{i}\tilde{\omega}_k\epsilon)\,\boldsymbol{e}_k\end{cases} \tag{B-3}$$

where

$$o_k = \sigma\cos\left[\frac{\pi}{N}(k-1)\right]\mathrm{SGN}(k) \tag{B-4}$$

o_k is symmetric with respect to k (i.e., $o_k = o_{N+2-k}$) and keeps positive over the range of index k. Otherwise, a negative o_k will bring about gain rather than loss—obviously it is in conflict with the Ohm-loss presumption.

Subsequently, the w-domain complex Poynting vector can be represented as

$$\boldsymbol{S}_{\mathrm{av}} = \frac{1}{N}\sum_{n=1}^{N}\boldsymbol{E}[n]\times\left(\frac{\boldsymbol{H}[n-1]+\boldsymbol{H}[n]}{2}\right) \tag{B-5}$$

Substituting the inverse transforms of (9) and (10) to (B-5) under the conjugate symmetric condition, we have

$$\boldsymbol{S}_{\mathrm{av}} = \frac{1}{N}\sum_{k=1}^{\lceil\frac{N+1}{2}\rceil}\delta_k\mathrm{Re}\left(\boldsymbol{e}_k\times\boldsymbol{h}_k^*\right)\cos\left[\frac{\pi}{N}(k-1)\right] \tag{B-6}$$

For odd N,

$$\delta_k = \begin{cases}1, & k=1\\ 2, & k=2,3,\dots,\dfrac{N+1}{2}\end{cases} \tag{B-7}$$

For even N,

$$\delta_k = \begin{cases}1, & k=1 \;\&\; \dfrac{N}{2}+1\\ 2, & k=2,3,\dots,\dfrac{N}{2}\end{cases} \tag{B-8}$$

In turn, the w-domain complex Poynting vector can be represented as

$$\boldsymbol{s} = \frac{1}{N}\sum_{k=1}^{\lceil\frac{N+1}{2}\rceil}\delta_k\left(\boldsymbol{e}_k\times\boldsymbol{h}_k^*\right)\cos\left[\frac{\pi}{N}(k-1)\right] \tag{B-9}$$

Inserting (B-3) to (B-9), we have

$$-\nabla\cdot\boldsymbol{s} = \mathrm{i}[p_e - p_m] + p_j \tag{B-10}$$

where

$$p_e = \frac{1}{N}\sum_{k=1}^{\lceil\frac{N+1}{2}\rceil}\delta_k\tilde{\omega}_k\epsilon|\boldsymbol{e}_k|^2\cos\left[\frac{\pi}{N}(k-1)\right] \tag{B-11}$$

$$p_m = \frac{1}{N}\sum_{k=1}^{\lceil\frac{N+1}{2}\rceil}\delta_k\tilde{\omega}_k\mu|\boldsymbol{h}_k|^2\cos\left[\frac{\pi}{N}(k-1)\right] \tag{B-12}$$

$$p_j = \frac{1}{N}\sum_{k=1}^{\lceil\frac{N+1}{2}\rceil}\delta_k o_k|\boldsymbol{e}_k|^2\cos\left[\frac{\pi}{N}(k-1)\right] \tag{B-13}$$

where p_e, p_m, and p_j denote the complex power density of electric field, that of magnetic field, and Ohm loss, respectively. Equation (B-10) describes and substantiates the conservation of energy in the w domain.

Appendix C. Transformation of Boundary Conditions

So far, we have only investigated the "volume" behavior of Maxwell's equations in the w domain, and we need to derive the boundary conditions so as to complete our theory.

Figure C-1 shows the interface of two different media with the corresponding EM physical quantities. The boundary conditions of Maxwell's equations in the discrete time domain are

$$\begin{aligned}&\hat{\boldsymbol{n}}\times(\boldsymbol{E}_1[n]-\boldsymbol{E}_2[n]) = 0\\ &\hat{\boldsymbol{n}}\times(\boldsymbol{H}_1[n]-\boldsymbol{H}_2[n]) = \boldsymbol{J}_s[n]\\ &\hat{\boldsymbol{n}}\cdot(\boldsymbol{D}_1[n]-\boldsymbol{D}_2[n]) = \varrho_s[n]\\ &\hat{\boldsymbol{n}}\cdot(\boldsymbol{B}_1[n]-\boldsymbol{B}_2[n]) = 0\end{aligned} \tag{C-1}$$

Accordingly, the w-domain correspondences of (C-1) are

$$\begin{aligned}&\hat{\boldsymbol{n}}\times(\boldsymbol{e}_{1k}-\boldsymbol{e}_{2k}) = 0\\ &\hat{\boldsymbol{n}}\times(\boldsymbol{h}_{1k}-\boldsymbol{h}_{2k}) = \boldsymbol{j}_{sk}\\ &\hat{\boldsymbol{n}}\cdot(\boldsymbol{d}_{1k}-\boldsymbol{d}_{2k}) = \rho_{sk}\\ &\hat{\boldsymbol{n}}\cdot(\boldsymbol{b}_{1k}-\boldsymbol{b}_{2k}) = 0\end{aligned} \tag{C-2}$$

where $\hat{\boldsymbol{n}}$ denotes the unit normal vector of the interface. $\boldsymbol{D}$ ($\boldsymbol{d}$) and $\boldsymbol{B}$ ($\boldsymbol{b}$) represent the electric and magnetic flux densities, respectively; $\boldsymbol{J}_s$ ($\boldsymbol{j}_s$) and ϱ_s (ρ_s) denote the electric current and charge density at the interface, respectively.

Especially, the w-domain boundary PEC and perfect magnetic conductor (PMC) can be expressed as

$$\boldsymbol{e}_k = 0 \tag{C-3}$$

and

$$\boldsymbol{h}_k = 0 \tag{C-4}$$

respectively. Equations (C-2)–(C-4) indicate that the w-domain boundary conditions are very similar to the frequency-domain ones, except the quantized feature. It implies that we can inherit the existing frequency-domain methods and derive their w-domain versions via a certain modification related to spectrum.

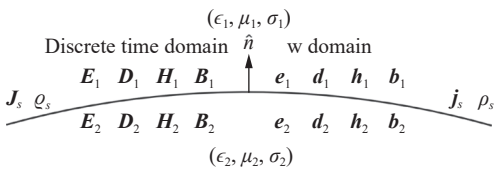

Figure C-1 Boundary conditions at the interface of two different materials: physical quantities in periodic-sequential domain (left side) and in the w domain (right side).

Appendix D. Field Expressions for TE_{mlk} Mode in RWG

In the w domain, the EM fields corresponding to the kth component in RWG are subject to

$$\begin{bmatrix} e_{x_k} \\ e_{y_k} \\ h_{x_k} \\ h_{y_k} \end{bmatrix} = \frac{1}{\kappa_c^2} \begin{bmatrix} \frac{\partial}{\partial z} & 0 & 0 & \mathrm{i}\tilde{\omega}_k\mu \\ 0 & \frac{\partial}{\partial z} & -\mathrm{i}\tilde{\omega}_k\mu & 0 \\ 0 & -\mathrm{i}\tilde{\omega}_k\epsilon & \frac{\partial}{\partial z} & 0 \\ \mathrm{i}\tilde{\omega}_k\epsilon & 0 & 0 & \frac{\partial}{\partial z} \end{bmatrix} \begin{bmatrix} \frac{\partial e_{z_k}}{\partial x} \\ \frac{\partial e_{z_k}}{\partial y} \\ \frac{\partial h_{z_k}}{\partial x} \\ \frac{\partial h_{z_k}}{\partial y} \end{bmatrix} \tag{D-1}$$

Under the PEC boundary condition (C-3), the TE_{mlk} mode of RWG can be derived as

$$\begin{aligned} h_{z_k} &= h_{ml}^k \cdot 1 \cdot \cos(\kappa_x^m x)\cos(\kappa_y^l y)\exp(\mathrm{i}\kappa_{z_k} z) \\ e_{x_k} &= h_{ml}^k \cdot \frac{-\mathrm{i}\mu\kappa_y^l\tilde{\omega}_k}{\kappa_c^2} \cdot \cos(\kappa_x^m x)\sin(\kappa_y^l y)\exp(\mathrm{i}\kappa_{z_k} z) \\ e_{y_k} &= h_{ml}^k \cdot \frac{\mathrm{i}\mu\kappa_x^m\tilde{\omega}_k}{\kappa_c^2} \cdot \sin(\kappa_x^m x)\cos(\kappa_y^l y)\exp(\mathrm{i}\kappa_{z_k} z) \\ h_{x_k} &= h_{ml}^k \cdot \frac{-\mathrm{i}\kappa_{z_k}}{\kappa_c^2} \cdot \sin(\kappa_x^m x)\cos(\kappa_y^l y)\exp(\mathrm{i}\kappa_{z_k} z) \\ h_{y_k} &= h_{ml}^k \cdot \frac{-\mathrm{i}\kappa_{z_k}}{\kappa_c^2} \cdot \cos(\kappa_x^m x)\sin(\kappa_y^l y)\exp(\mathrm{i}\kappa_{z_k} z) \end{aligned} \tag{D-2}$$

Here, m and l represent the modal indices of $\hat{x}$ and $\hat{y}$ directions, respectively. h_{ml}^k is the magnetic field intensity of the input periodic sequence. $\kappa_x^m = m\pi/a$, $\kappa_y^l = l\pi/b$, and $\kappa_c = \sqrt{(\kappa_x^m)^2 + (\kappa_y^l)^2}$. κ_{z_k} denotes the dispersion relation of RWG in the w domain.

Suppose that only $\{TE_{10k}\}$ $(k = 1, 2, \ldots, k_{max})$ modes are allowed to propagate along the waveguide, i.e.,

$$\frac{\pi}{a} < \frac{2\sqrt{\epsilon\mu}}{\Delta t}\sin\left[\frac{\pi}{N}(k_{\max} - 1)\right] < \frac{2\pi}{a} \tag{D-3}$$

where $k_{\max}$ denotes the maximum index of the nonzero components. In the traditional frequency domain, "TE_{10}" represents the main mode of RWG; while in the w domain, we define "TE_{10k}" as the main mode and "TE_{10}" denotes the complete set of TE_{10k} $(k = 1, 2, \ldots, k_{\max})$. Assuming that the highest frequency of the input signal equals to $f_{\max}$, we can take $(k_{\max} - 1)/T$ as its approximation. Note that the sampling interval Δt will be decided not only by Nyquist sampling condition but also the main-modes-only condition (D-3):

$$\frac{T \cdot \mathrm{Sa}^{-1}[\min(1, C)]}{\pi(k_{\max} - 1)} < \Delta t < \frac{T \cdot Sa^{-1}\left[\max\left(\frac{2}{\pi}, \frac{C}{2}\right)\right]}{\pi(k_{\max} - 1)} \tag{D-4}$$

where $C = T/[(k_{\max} - 1)a\sqrt{\epsilon\mu}]$. Specifically, when the quantized spectrum of input sequence is relatively narrow $\frac{T}{2a\sqrt{\epsilon\mu}} + 1 < k_{\max} < \frac{T\pi}{4a\sqrt{\epsilon\mu}} + 1$, the propagation condition of TE_{10} modes will dominate the upper bound of Δt. With the increase of the bandwidth but still within the range $\frac{T\pi}{4a\sqrt{\epsilon\mu}} + 1 < k_{\max} < \frac{T}{a\sqrt{\epsilon\mu}} + 1$, the upper bound will be decided by unaliasing sampling condition. Once $k_{\max} > \frac{T}{a\sqrt{\epsilon\mu}} + 1$, the lower bound will be controlled by the TE_{20}-modes cutoff condition.

References

[1] A. Momeni and R. Fleury, "Electromagnetic wave-based extreme deep learning with nonlinear time-floquet entanglement," *Nature Communications*, vol. 13, no. 1, article no. 2651, 2022.

[2] M. Mirhosseini, E. Kim, V. S. Ferreira, *et al.*, "Superconducting metamaterials for waveguide quantum electrodynamics," *Nature Communications*, vol. 9, no. 1, article no. 3706, 2018.

[3] W. W. Zhu, H. R. Xue, J. B. Gong, *et al.*, "Time-periodic corner states from floquet higher-order topology," *Nature Communications*, vol. 13, no. 1, article no. 11, 2022.

[4] P. N. Butcher, "A natural form for large amplitude time-periodic acoustic travelling waves in piezoelectric semiconductors," *Journal of Physics C: Solid State Physics*, vol. 4, no. 1, pp. 36–43, 1971.

[5] T. Valier-Brasier, C. Potel, and M. Bruneau, "Pressure and shear horizontal guided waves excitation: Nonuniform, time-periodic source distribution of finite extent on the boundaries," *Applied Physics Letters*, vol. 98, no. 15, article no. 154102, 2011.

[6] W. Kohn, "Periodic thermodynamics," *Journal of Statistical Physics*, vol. 103, no. 3, pp. 417–423, 2001.

[7] H. Karatas and T. Derbentli, "Natural convection in differentially heated rectangular cavities with time periodic boundary condition on one side," *International Journal of Heat and Mass Transfer*, vol. 129, pp. 224–237, 2019.

[8] N. Nithyadevi, P. Kandaswamy, and S. M. Sundari, "Magnetoconvection in a square cavity with partially active vertical walls: Time periodic boundary condition," *International Journal of Heat and Mass Transfer*, vol. 52, no. 7–8, pp. 1945–1953, 2009.

[9] P. C. Lingos, M. D. Kapetanakis, J. G. Wang, *et al.*, "Light-wave control of correlated materials using quantum magnetism during time-periodic modulation of coherent transport," *Communications Physics*, vol. 4, no. 1, article no. 60, 2021.

[10] S. F. Tian and T. T. Zhang, "Long-time asymptotic behavior for the Gerdjikov-Ivanov type of derivative nonlinear Schrödinger equation with time-periodic boundary condition," *Proceedings of the American Mathematical Society*, vol. 146, no. 4, pp. 1713–1729, 2018.

[11] L. Reichl, "Time-periodic quantum systems," in *The Transition to Chaos: Conservative Classical and Quantum Systems*, L. Reichl, Ed. Springer, Cham, Switzerland, pp. 339–396, 2021.

[12] K. Yee, "Numerical solution of initial boundary value problems involving Maxwell's equations in isotropic media," *IEEE Transactions on Antennas and Propagation*, vol. 14, no. 3, pp. 302–307, 1966.

[13] T. K. Jensen, "On adaptive wavelet-based methods for the Maxwell equations, " *Ph.D. Thesis*, Dept. Math., Technical University of Denmark, Copenhagen, The Kingdom of Denmark, 2003.

[14] Y. S. Chung, T. K. Sarkar, B. H. Jung, *et al.*, "Solution of time domain electric field integral equation using the Laguerre polynomials," *IEEE Transactions on Antennas and Propagation*, vol. 52, no. 9, pp. 2319–2328, 2004.

[15] A. Christ and H. L. Hartnagel, "Three-dimensional finite-difference method for the analysis of microwave-device embedding," *IEEE Transactions on Microwave Theory and Techniques*, vol. 35, no. 8, pp. 688–696, 1987.

[16] R. Harrington, "Origin and development of the method of moments for field computation," *IEEE Antennas and Propagation Magazine*, vol. 32, no. 3, pp. 31–35, 1990.

[17] J. M. Jin, *The Finite Element Method in Electromagnetics*, 3rd ed., John Wiley & Sons, Hoboken, NJ, USA, 2014.

[18] O. Heaviside, "Sound waves and electromagnetics. The pan-potential," *Nature*, vol. 67, no. 1731, pp. 202–203, 1903.
[19] J. A. McWilliams, "Electromagnetics: A discussion of fundamentals," *Thought: Fordham University Quarterly*, vol. 14, no. 4, pp. 677–680, 1939.
[20] A. H. M. Arnold, "Electromagnetics," *Nature*, vol. 206, no. 4991, article no. 1282, 1965.
[21] D. K. Cheng, *Fundamentals of Engineering Electromagnetics*. Addison-Wesley, New York, NY, USA, 1993.
[22] J. D. Jackson, *Classical Electrodynamics*. Wiley, New York, NY, USA, 1999.
[23] R. Pregla, *Analysis of Electromagnetic Fields and Waves: The Method of Lines*. John Wiley & Sons, Hoboken, NJ, USA, 2008.
[24] R. Pregla, "Higher order approximation for the difference operators in the method of lines," *IEEE Microwave and Guided Wave Letters*, vol. 5, no. 2, pp. 53–55, 1995.
[25] P. B. Monk and A. K. Parrott, "A dispersion analysis of finite element methods for Maxwell's equations," *SIAM Journal on Scientific Computing*, vol. 15, no. 4, pp. 916–937, 1994.
[26] J. C. Nedelec, "Mixed finite elements in R^3," *Numerische Mathematik*, vol. 35, no. 3, pp. 315–341, 1980.
[27] J. F. Lee, D. K. Sun, and Z. J. Cendes, "Full-wave analysis of dielectric waveguides using tangential vector finite elements," *IEEE Transactions on Microwave Theory and Techniques*, vol. 39, no. 8, pp. 1262–1271, 1991.
[28] S. Boyd and L. Vandenberghe, *Convex Optimization*. Cambridge University Press, Cambridge, UK, 2004.

Ben You received the M.S. degree in electronic science and technology from Shanghai Jiao Tong University, Shanghai, China, in 2017, and Ph.D. degree from Polytechnique Montreal, Montreal, Canada, in 2023. His current research interests include the modeling of radio frequency tranceiver (Tx) and receiver (Rx) system and electronic design automation (EDA) with artificial intelligence (AI). He is currently working as a postdoctoral researcher with Shanghai Jiao Tong University, focusing on EDA-AI research, starting from 2024.
(Email: youben917@sjtu.edu.cn)

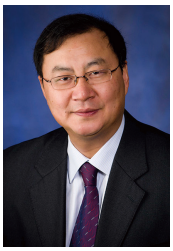

Ke Wu received the B.S. degree (Hons.) in radio engineering from Nanjing Institute of Technology (now Southeast University), Nanjing, China, in 1982, the D.E.A. degree (Hons.) and the Ph.D. degree (Hons.) in optics, optoelectronics, and microwave engineering, respectively in 1984 and 1987, all from the Institut National Polytechnique de Grenoble (INPG) and the University of Grenoble, Grenoble, France.

He was the Founding Director of the Center for Radio Frequency Electronics Research of Quebec (Regroupement stratégique of FRQNT) and the Canada Research Chair of RF and millimeter-wave engineering. He is currently a Professor of electrical engineering and the Industrial Research Chair in Future Wireless Technologies with the Polytechnique Montréal (University of Montreal), where he was the Director of the Poly-Grames Research Center from 1998 to 2024. He has (co)authored over 1500 referred articles and numerous books/book chapters and filed over 90 patents. His current research interests involve substrate integration technologies, antenna arrays, field theory and joint field/circuit modeling, ultrafast guided-wave electronics, wireless power transfer and harvesting, microwave photonics, and MHz-through-THz technologies and transceivers including radio frequency integrated circuits (RFICs) / monolithic microwave integrated circuits (MMICs) for joint radar/communication architectures, innovative multifunction wireless systems, and biomedical applications.

Dr. Wu is a Fellow of the Canadian Academy of Engineering, the Academy of Science of the Royal Society of Canada, and the German National Academy of Science and Engineering (acatech). He is a member of the Electromagnetics Academy, Union Radio-Scientifique Internationale (URSI), and IEEE-Eta Kappa Nu (IEEE-HKN). He was a recipient of many awards and prizes including the inaugural IEEE MTT-S Outstanding Young Engineer Award, the 2004 Fessenden Medal of the IEEE Canada, the 2009 Thomas W. Eadie Medal of the Royal Society of Canada, the Queen Elizabeth II Diamond Jubilee Medal in 2013, the 2013 Fellow of the College of Chest Physicians (FCCP) Education Foundation Award of Merit, the 2014 IEEE MTT-S Microwave Application Award, the 2014 Marie-Victorin Prize (Prix du Quebec), the 2015 Prix d'Excellence en Recherche et Innovation of Polytechnique Montréal, the 2015 IEEE Montreal Section Gold Medal of Achievement, the 2019 IEEE MTT-S Microwave Prize, the 2021 Engineering Institute of Canada (EIC) Julian C. Smith Medal, the 2022 IEEE MTT-S Outstanding Educator Award, and the 2022 IEEE Antennas and Propagation Society (AP-S) John Kraus Antenna Award. He has held key positions in and has served on various panels and international committees including the Chair of technical program committees, international steering committees, and international conferences/symposia. In particular, he was the General Chair of the 2012 IEEE Microwave Theory and Techniques (IEEE MTT-S) International Microwave Symposium (IMS) and technical program committee (TPC) Co-Chair of the 2020 IEEE International Symposium on Antennas and Propagation (APS). He has served on the editorial/review boards for many technical journals, transactions, proceedings, and letters as well as scientific encyclopedia including editor, track editor, and guest editor. He was the Chair of the joint IEEE Montreal chapters of MTT-S/AP-S/Lasers and Electro-Optics Society (LEOS) and then the restructured IEEE MTT-S Montreal Chapter, Canada. He has served the IEEE MTT-S Administrative Committee (AdCom) as the Chair for the IEEE MTT-S Transnational Committee, the Member and Geographic Activities (MGA) Committee, Technical Coordinating Committee (TCC), and the 2016 IEEE MTT-S President among many other AdCom functions. He is currently the Chair of the IEEE MTT-S Inter-Society Committee. He was a Distinguished Microwave Lecturer of the IEEE MTT-S from 2009 to 2011. He served the European Microwave Association (EuMA) as the Inaugural Representative of North America in its General Assembly.
(Email: ke.wu@polymtl.ca)